JACS
JOURNAL OF THE AMERICAN CHEMICAL SOCIETY
pubs.acs.org/JACS
Article

Ethane/Ethylene Separations in Flexible Diamondoid Coordination Networks via an Ethane-Induced Gate-Opening Mechanism

Shao-Min Wang, Mohana Shivanna, Su-Tao Zheng, Tony Pham, Katherine A. Forrest, Qing-Yuan Yang,* Qingqing Guan,* Brian Space, Susumu Kitagawa, and Michael J. Zaworotko*

Cite This: J. Am. Chem. Soc. 2024, 146, 4153−4161

ABSTRACT: Separating ethane (C_2H_6) from ethylene (C_2H_4) is an essential and energy-intensive process in the chemical industry. Here, we report two flexible diamondoid coordination networks, **X-dia-1-Ni** and **X-dia-1-Ni$_{0.89}$Co$_{0.11}$**, that exhibit gate-opening between narrow-pore (NP) and large-pore (LP) phases for C_2H_6, but not for C_2H_4. **X-dia-1-Ni$_{0.89}$Co$_{0.11}$** thereby exhibited a type F−IV isotherm at 273 K with no C_2H_6 uptake and a high uptake (111 cm^3 g^{-1}, 1 atm) for the NP and LP phases, respectively. Conversely, the LP phase exhibited a low uptake of C_2H_4 (12.2 cm^3 g^{-1}). This C_2H_6/C_2H_4 uptake ratio of 9.1 for **X-dia-1-Ni$_{0.89}$Co$_{0.11}$** far surpassed those of previously reported physisorbents, many of which are C_2H_4-selective. *In situ* variable-pressure X-ray diffraction and modeling studies provided insight into the abrupt C_2H_6-induced structural NP to LP transformation. The promise of pure gas isotherms and, more generally, flexible coordination networks for gas separations was validated by dynamic breakthrough studies, which afforded high-purity (99.9%) C_2H_4 in one step.

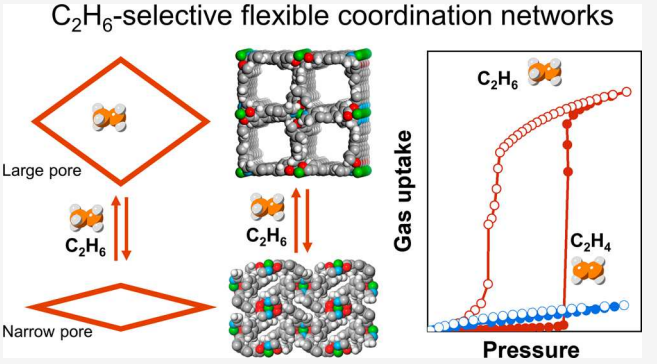

INTRODUCTION

Third-generation porous coordination polymers (PCPs) such as soft porous crystals (SPCs) or flexible metal−organic frameworks (FMOFs) are gaining attention because their stimuli-induced structural transformations can selectively respond to various guests.[1,2] That they can undergo such transformations distinguishes them from traditional solid physisorbents such as zeolites, aluminum oxides, activated carbons, and rigid MOFs. Among the >118,000 MOFs reported thus far, only ∼1000 are known to exhibit structural flexibility and dynamic behavior[3,4] that could be suitable for applications such as gas storage,[5,6] catalysis,[7,8] separation,[9−11] sensing,[12,13] and drug delivery.[14,15] FMOFs undergo structural transformations due to an external stimulus, most commonly by controlling the sorbate pressure.[16−18]

Adsorption-induced gate-opening is perhaps the most commonly observed phenomenon in FMOFs, and it demonstrates their potential utility in next-generation gas storage and separation technologies.[19,20] For example, Li's group reported an FMOF, Mn(ina)$_2$, that exhibited a temperature-controlled response to the adsorption of rare-gas molecules. This sorbent reached its maximum uptake of rare gas at a specific temperature threshold, leading to inversion of the Xe/Kr adsorption selectivity as a function of temperature.[11] Among commodity chemicals, ethylene (C_2H_4) plays a significant role in the petrochemical industry for the production of polyethylene and polyvinyl chloride, which are used in textiles and plastics.[21] Currently, C_2H_4 is mainly produced by steam cracking of naphtha, which inevitably introduces undesired impurities such as ethane (C_2H_6), thereby reducing the purity level below that required for ethylene polymerization. C_2H_4/C_2H_6 separation is challenging because of their similar physicochemical properties (Table S1). The cryogenic distillation C_2H_4/C_2H_6 separation process operates at high pressures (5−28 bar) and low temperatures (180−258 K) and comes with a significant energy footprint.[22,23] In principle, adsorption separation can overcome the shortcomings of cryogenic distillation and thus holds promise for industrial production.[24,25] Conventional solid porous adsorbents such as porous carbon materials[26] and zeolites[27] have been studied extensively in ethylene/ethane separations. However, their relatively low adsorption capacities and selectivities do not meet the requirements for application.

Due to their variable compositions, pore structures, and properties, MOFs, both flexible and rigid, offer promise to

Received: November 22, 2023
Revised: January 18, 2024
Accepted: January 19, 2024
Published: February 1, 2024

https://doi.org/10.1021/jacs.3c13117
J. Am. Chem. Soc. 2024, 146, 4153−4161

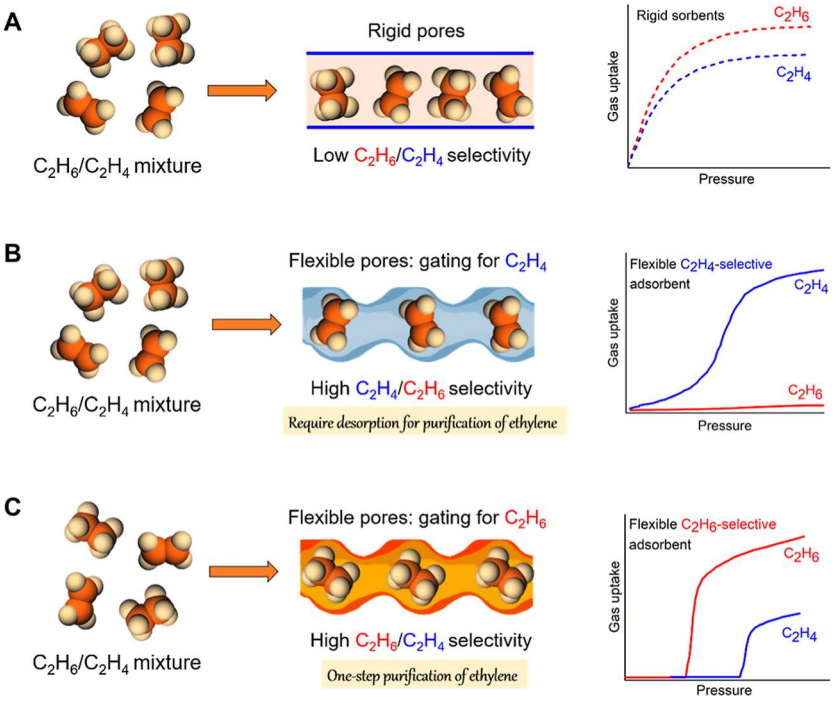

Figure 1. Illustration of rigid and flexible MOF adsorbents for ethane/ethylene selective adsorption. (A) Rigid MOFs tend to show little adsorption difference between C_2H_4 and C_2H_6. (B) Flexible C_2H_4-selective porous materials need an additional desorption process to release adsorbed C_2H_4. (C) Flexible C_2H_6-selective porous materials are the most suitable for C_2H_6/C_2H_4 separations.

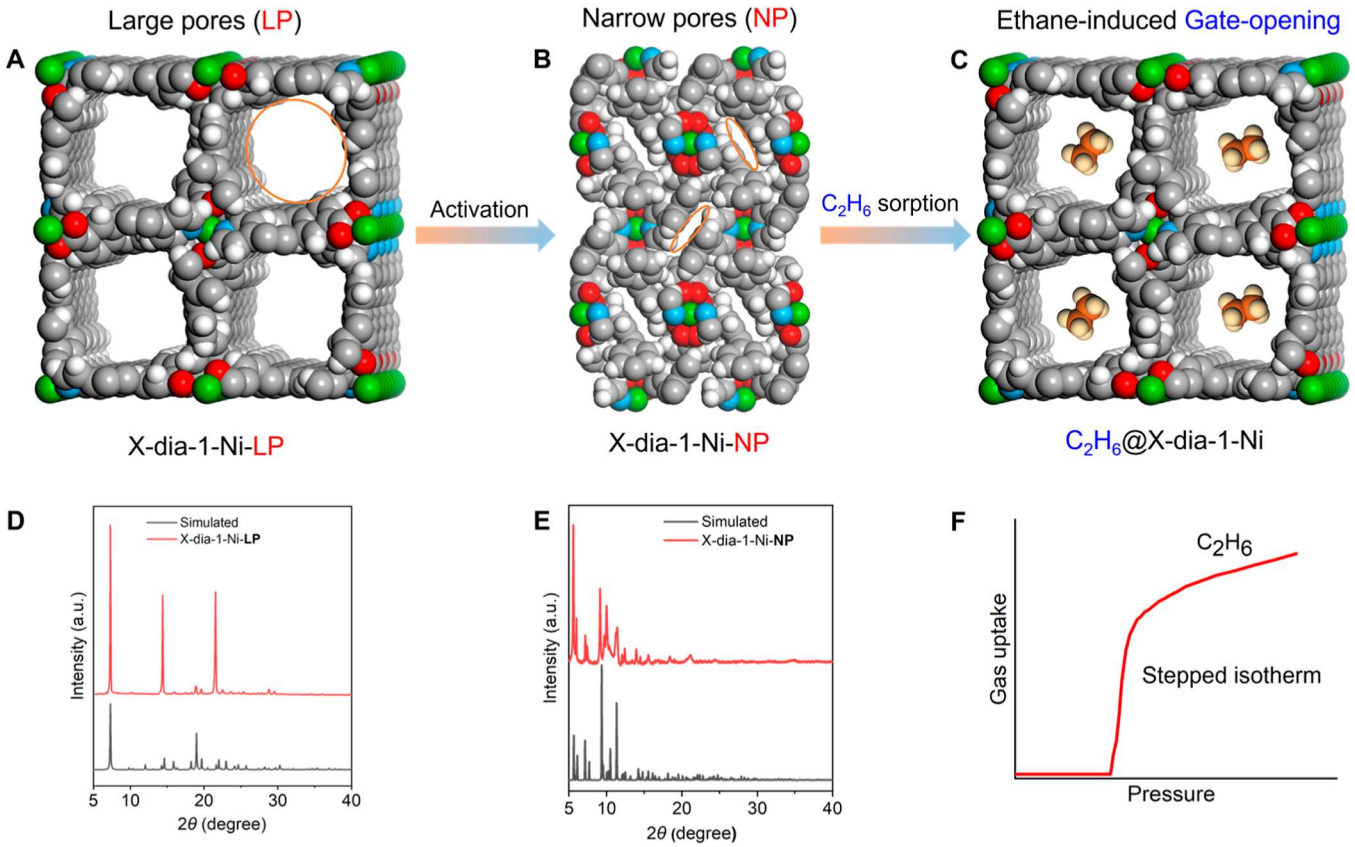

Figure 2. (A,B) Illustrations of the pore structure of the LP and NP phases of **X-dia-1-Ni**, respectively. (C) C_2H_6 adsorption induced the structural transformation of **X-dia-1-Ni**. (D) PXRD patterns for the LP phases, **X-dia-1-Ni**-LP. (E) PXRD patterns of the NP phases, **X-dia-1-Ni**-NP. (F) Ethane-induced stepped isotherm.

https://doi.org/10.1021/jacs.3c13117
J. Am. Chem. Soc. 2024, 146, 4153−4161

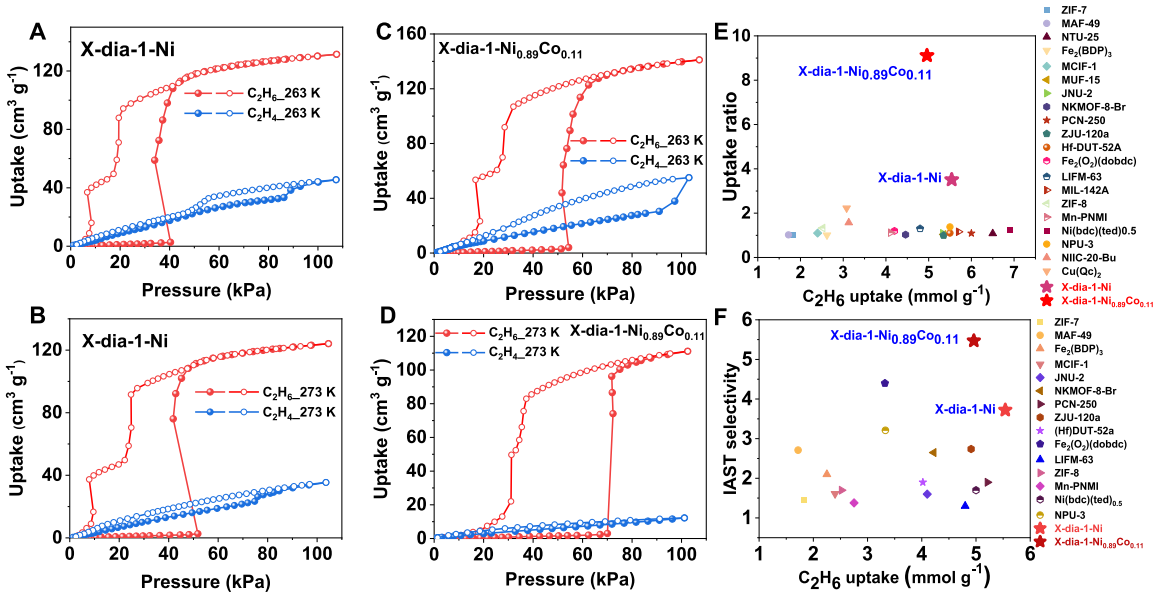

Figure 3. C_2H_4 and C_2H_6 adsorption isotherms for (A) **X-dia-1-Ni** at 263 K, (B) **X-dia-1-Ni** at 273 K, (C) **X-dia-1-Ni$_{0.89}$Co$_{0.11}$** at 263 K, and (D) **X-dia-1-Ni$_{0.89}$Co$_{0.11}$** at 273 K. (E) Comparisons of C_2H_6/C_2H_4 uptake ratios with values obtained for previously reported sorbents. (F) Comparison of IAST selectivities with literature values (the values for **X-dia-1-Ni** and **X-dia-1-Ni$_{0.89}$Co$_{0.11}$** were calculated at 273 K).

address the aforementioned separation challenges.[28−33] Nevertheless, separating C_2H_6 from C_2H_4 remains a particular challenge because most sorbents are selective for C_2H_4 because of its unsaturated nature which can in turn require a high-energy footprint for C_2H_4 removal. Therefore, it is desirable to design and study adsorbents with "inverse selectivity", which, if strongly C_2H_6-selective, could reduce energy footprints by up to 40%.[23,34−36] The current generation of C_2H_6-selective MOFs tends to be rigid and typically exhibit low C_2H_6/C_2H_4 selectivities (<2) and low C_2H_6/C_2H_4 uptake ratios of just above 1.[37−39] Among them, $Fe_2(O_2)$(dobdc) exhibits high C_2H_6/C_2H_4 selectivity owing to the role of Fe-peroxo sites in preferential interactions with C_2H_6, but the C_2H_6 uptake is relatively low.[40] Although vanadium and titanium MOFs can exhibit high C_2H_6 uptake through pore-space partition,[41] their C_2H_6/C_2H_4 selectivities are also relatively low. While the rigid MOFs mentioned above are promising, they do not offer high uptake capacity and high selectivity.

Compared to rigid C_2H_6-selective adsorbents, FMOFs can selectively open their pores to admit gases, depending on the strength of host−guest interactions and temperature. Thus, flexible porous materials exhibiting tunable gate-opening could exhibit unexpectedly high C_2H_6/C_2H_4 selectivities (Figure 1). Recently, Chen et al. prepared a flexible porous material (HOF-FJU-1) to separate C_2H_4 and C_2H_6 through a gating mechanism.[42] Nevertheless, HOF-FJU-1, although flexible, is C_2H_4-selective, and a desorption process is needed to obtain pure C_2H_4. In 2010, Gucuyener et al. reported a microporous material, ZIF-7, displaying selective C_2H_6 adsorption over C_2H_4. However, ZIF-7 showed similar gate-opening pressures for C_2H_6 and C_2H_4, resulting in a comparable uptake for C_2H_6 and C_2H_4.[43]

In this study, we report on the C_2H_6 and C_2H_4 sorption behavior of two previously reported FMOFs, **X-dia-1-Ni** and **X-dia-1-Ni$_{0.89}$Co$_{0.11}$**, which exhibit methane-induced gate-opening at relatively low pressures.[17] In particular, we observed that **X-dia-1-Ni$_{0.89}$Co$_{0.11}$** exhibits a significant difference in its C_2H_6 and C_2H_4 uptake at near ambient conditions with the highest C_2H_6/C_2H_4 uptake ratio reported yet. Adsorption isotherms, breakthrough experiments, *in situ* variable-pressure powder X-ray diffraction (PXRD) measurements, and theoretical calculations were used to provide insight into the C_2H_6/C_2H_4 separation performance under dynamic conditions.

RESULTS AND DISCUSSION

Structure, Stability, and Flexibility. The hydrothermal reaction between nickel(II) nitrate hexahydrate and 4-(4-pyridyl)-biphenyl-4-carboxylic acid (L) afforded **X-dia-1-Ni** as reported previously (Figure S1). The experimental procedure is provided in the Supporting Information. The pore structures of the large pore (LP) and narrow pore (NP) phases are shown in Figure 2A ,B. As revealed by Figure 2C,D, the phase purity of the as-synthesized material was verified by comparing experimental and calculated PXRD data. **X-dia-1-Ni** underwent a single-crystal to single-crystal transformation from an LP phase (**X-dia-1-Ni-LP**) to an NP phase (**X-dia-1-Ni-NP**) upon exchange with dichloromethane and heating at 45 °C for 20 h. The PXRD pattern for **X-dia-1-Ni-NP** was consistent with that calculated from the single-crystal structure (Figure 2D). **X-dia-1-Ni$_{0.89}$Co$_{0.11}$**, which is isomorphous to **X-dia-1-Ni**, was synthesized under the same condition by adjusting the Ni^{2+} and Co^{2+} concentrations. The PXRD patterns for both the as-synthesized and activated phases match those of the Ni parent. Fourier transform infrared (FTIR) spectra (Figures S2 and S3) of **X-dia-1-Ni** and **X-dia-1-Ni$_{0.89}$Co$_{0.11}$** showed characteristic peaks that we ascribe to the framework moieties. Thermogravimetric analysis (TGA) profiles revealed weight losses corresponding to the guest molecules in the pores (Figures S4 and S5). Below 200 °C, the TGA curves obtained under N_2 for **X-dia-1-Ni** and **X-dia-1-Ni$_{0.89}$Co$_{0.11}$** indicated weight losses of 35.2 and 30%, respectively. The N_2 (77 K) and CO_2 (195 K) adsorption isotherms were measured to check the flexibility and porosity of **X-dia-1-Ni** (Figure S6). **X-dia-1-Ni** did not adsorb N_2 at 77 K and showed multistep adsorption of CO_2 at 195 K. As expected, **X-dia-1-Ni$_{0.89}$Co$_{0.11}$** showed

https://doi.org/10.1021/jacs.3c13117
J. Am. Chem. Soc. 2024, 146, 4153−4161

multistep adsorption of CO_2 at 195 K and negligible N_2 uptake at 77 K (Figure S7), consistent with our previous study of **X-dia-1-Ni**.[17] The multistep CO_2 adsorption behavior of **X-dia-1-Ni$_{0.89}$Co$_{0.11}$** can be attributed to a phase transformation from the NP phase to at least two LP phases, three of which were identified.[17]

Single-Component Gas Adsorption. We measured the single−component isotherms for C_2H_6 and C_2H_4 adsorption by **X-dia-1-Ni** at 263, 273, and 298 K. Before the adsorption measurements, **X-dia-1-Ni-LP** (fully open) was exchanged with CH_2Cl_2 and evacuated under dynamic vacuum to afford **X-dia-1-Ni-NP**. At low pressures (<40.3 kPa), the NP phase was nonporous to C_2H_6 adsorption at 263 K (Figure 3A) but phase transformation to the LP phase occurred at 40.3 kPa. C_2H_6 uptake then jumped abruptly with increasing pressure and plateaued at ca. 100 kPa. The C_2H_6 adsorption capacity at 263 K was determined to be 131.4 cm^3 g^{-1}. Conversely, the NP phase was porous to C_2H_4 adsorption at 263 K, but there was no evident gate-opening and an uptake of 44.8 cm^3 g^{-1} (Figure 3A). In effect, the NP phase is a sieve for C_2H_6 and could exhibit transient porosity to enable gate-opening.[44] We next measured the adsorption isotherms of C_2H_6 and C_2H_4 at 273 K. For both gases, the adsorption capacity decreased. At 273 K, the pressure of C_2H_6 required for gate-opening in **X-dia-1-Ni** increased to 51.7 kPa (Figure 3B). **X-dia-1-Ni**, therefore, maintained its preferential adsorption toward C_2H_6 over C_2H_4, with uptake values of 124.1 and 35.4 cm^3 g^{-1}, respectively. The C_2H_6/C_2H_4 uptake ratio for **X-dia-1-Ni** at 273 K was found to be 3.51, higher than that for $Fe_2(O_2)(dobdc)$[40] and $Cu(Qc)_2$[45] at 273 or 298 K, the current benchmark C_2H_6-selective sorbents. At 298 K, **X-dia-1-Ni** did not exhibit gate-opening for either C_2H_6 or C_2H_4 below 1 atm (Figure S8). The gate-opening pressures of **X-dia-1-Ni** for the adsorption of C_2H_6 and C_2H_4 are presented in Table S2. Such temperature-dependent gate-opening has been seen in other FMOFs.[11]

For **X-dia-1-Ni$_{0.89}$Co$_{0.11}$**, the C_2H_6- and C_2H_4-induced gate-opening pressures increased, further confirming that the threshold pressures can be adjusted by varying the ratios of Ni/Co.[46−48] Reducing the energy barrier required for phase transformation was the motivation for replacing Ni with Co.[49] At 263 K, the pressure required for gate-opening of **X-dia-1-Ni$_{0.89}$Co$_{0.11}$** by C_2H_6 was 54.4 kPa (Figure 3C). It is worth noting that neither **X-dia-1-Co** nor **X-dia-1-Ni$_{0.32}$Co$_{0.68}$** adsorbed C_2H_6 or C_2H_4, and they did not exhibit gate-opening at 263 or 273 K (Figures S9−S12). In the following, we discuss the influence of Ni/Co ratios on the gate-opening pressure. It is known that the spin configuration significantly impacts the geometry of Co complexes.[50] In our previous work,[49] we explained how metal doping modulates the gate-opening pressure for methane adsorption in **X-dia-1-Ni$_x$Co$_{1-x}$**. The results showed that the energy barrier between the NP and LP phases for **X-dia-1-Co** was calculated to be higher than that for **X-dia-1-Ni**. It has been demonstrated in prior research that the metal component can impact gate-opening due to the difference in energy penalty for phase transformation.[46−48] While **X-dia-1-Ni$_x$Co$_{1-x}$** was found to exhibit similarities in adsorption of ethane to that of methane at high pressure, **X-dia-1-Co** exhibited minimal affinity for ethane at a low temperature. Our observation that with increasing Ni^{2+} content the opening pressure for ethane adsorption on **X-dia-1-Ni$_x$Co$_{1-x}$** gradually decreases is consistent with previous literature on this subject, which suggests that Co^{2+} nodes are more resistant to distortion than analogous Ni^{2+} nodes.

The amount of C_2H_6 adsorbed by **X-dia-1-Ni$_{0.89}$Co$_{0.11}$** was found to be 141.08 cm^3 g^{-1} at 263 K and 100 kPa, while the C_2H_4 uptake was only 55.1 cm^3 g^{-1} (Figure 3C). As the temperature was increased to 273 K, the threshold pressure of the step for C_2H_6 increased, whereas no step was observed during C_2H_4 adsorption. Therefore, the potential for separation of C_2H_6 from C_2H_4 was suggested by the pure gas sorption data for **X-dia-1-Ni$_{0.89}$Co$_{0.11}$** at 273 K (Figure 3D). As illustrated in Figure 3D, the uptake of C_2H_6 by **X-dia-1-Ni$_{0.89}$Co$_{0.11}$** at 273 K was approximately 9.1 times that of C_2H_4 (Figure 3D), suggesting high selectivity for C_2H_6. For context, the C_2H_6/C_2H_4 uptake ratio of the previous benchmark MOF, $Cu(Qc)_2$, was reported to be ca. 2 at 298 K and 100 kPa.[45]

Kinetic studies were conducted by directly pressurizing the system to 100 or 60 kPa. The maximum adsorption rate for C_2H_6 was 5.3 cm^3 g^{-1} s^{-1} (Figure S13), while the maximum adsorption rate for C_2H_4 was 2.33 cm^3 g^{-1} s^{-1} at 100 kPa (Figure S14). When the inlet pressure was reduced to 60 kPa, the maximum adsorption rates for C_2H_6 and C_2H_4 decreased to 2.09 and 1.44 cm^3 g^{-1} s^{-1} (Figures S15 and S16), respectively. These results show that **X-dia-1-Ni** exhibits different adsorption affinities for C_2H_6 and C_2H_4. Excellent cycling and reproducibility are required for practical applications, so multicycle adsorption−desorption tests were conducted to evaluate the recyclability of **X-dia-1-Ni** (Figure S17). These tests revealed that **X-dia-1-Ni** maintained its C_2H_6 uptake over five adsorption−desorption cycles. In addition, Figure S18 shows that the first and fifth C_2H_6 adsorption−desorption cycle curves exhibited almost the same shapes.

We also calculated and compared the C_2H_6/C_2H_4 uptake ratios with those of benchmark MOFs (Figure 3E and Table S4). **X-dia-1-Ni$_{0.89}$Co$_{0.11}$** has a remarkably high C_2H_6/C_2H_4 uptake ratio of 9.1 at 273 K and 1 bar, which is higher than that of **X-dia-1-Ni** (3.51). **X-dia-1-Ni** and **X-dia-1-Ni$_{0.89}$Co$_{0.11}$** also displayed very high IAST selectivities at 1 bar for binary C_2H_6/C_2H_4 (1/1 or 1/9, v/v) mixtures. The calculated IAST selectivities of **X-dia-1-Ni** for C_2H_6/C_2H_4 (1/1 or 1/9, v/v) were determined to be 3.72 and 2.52 at 273 K and 100 kPa (Figure S19), respectively. Figures S20 and S21 present the mixed-gas isotherms over **X-dia-1-Ni**, as predicted by IAST at different ratios of C_2H_6 to C_2H_4. The predicted C_2H_6 and C_2H_4 uptake values for a 1/1 ratio of C_2H_6 to C_2H_4 were 36.6 and 10.1 cm^3 g^{-1}. At a ratio of 1/9 (C_2H_6/C_2H_4), the C_2H_6 and C_2H_4 uptake values, respectively, decreased to 2.1 and 7.7 cm^3 g^{-1}. For **X-dia-1-Ni$_{0.89}$Co$_{0.11}$**, the IAST selectivities of C_2H_6/C_2H_4 (1/1 or 1/9, v/v) were determined to be 5.47 and 3.98, respectively (Figure S22), significantly higher than that of existing sorbents (Figure 3F). The IAST-predicted mixed-gas isotherms for **X-dia-1-Ni$_{0.89}$Co$_{0.11}$** at different ratios of C_2H_6 concerning C_2H_4 are shown in Figures S23 and S24. The predicted uptake values of C_2H_6 and C_2H_4 on **X-dia-1-Ni$_{0.89}$Co$_{0.11}$** at a 1/1 ratio of C_2H_6 to C_2H_4 were 46.8 and 8.7 cm^3 g^{-1}, respectively. At a ratio of 1/9, the amounts of adsorbed C_2H_6 and C_2H_4 decreased to 5.5 and 12.7 cm^3 g^{-1}, respectively. These values once again suggest that **X-dia-1-Ni$_{0.89}$Co$_{0.11}$** is a candidate for separating C_2H_6 from C_2H_4 in 1/9 ratios. Remarkably, ΔQ, which refers to the difference in uptake capacity between C_2H_6 and C_2H_4 at 1 bar in **X-dia-1-Ni$_{0.89}$Co$_{0.11}$**, is as high as 4.41 mmol g^{-1} (Figure S25). This

https://doi.org/10.1021/jacs.3c13117
J. Am. Chem. Soc. 2024, 146, 4153−4161

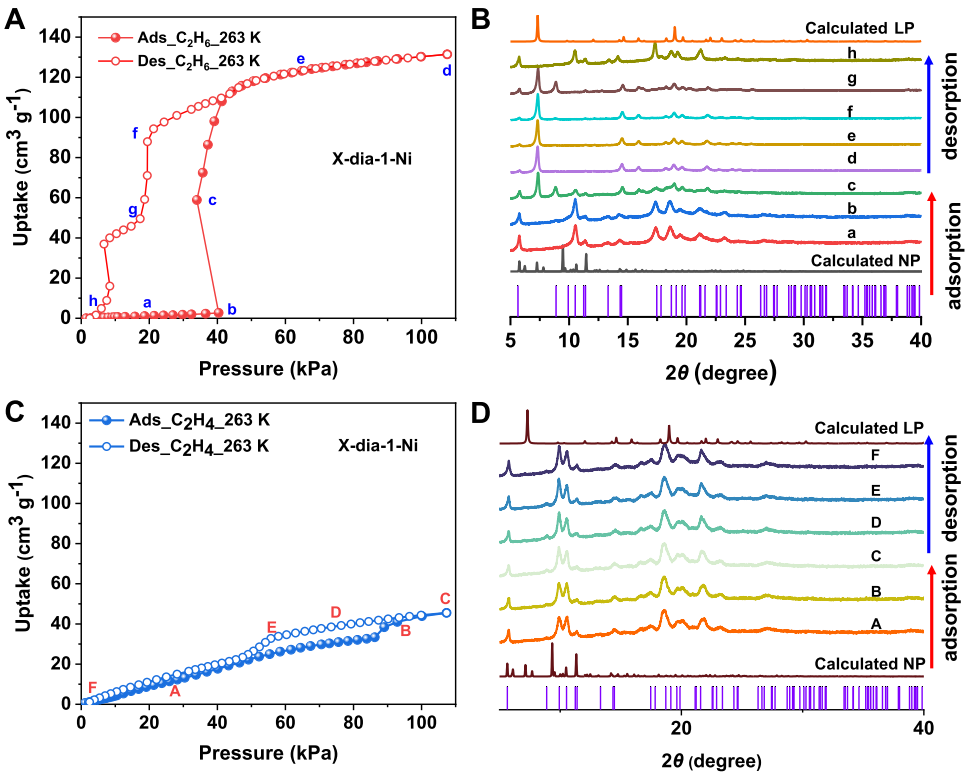

Figure 4. (A,B) Comparison of selected patterns after ethane adsorption and desorption at 263 K. **X-dia-1-Ni** underwent a reversible transformation from an NP phase to an LP phase upon dosing with ethane. (C,D) In situ PXRD patterns collected at 263 K, indicating that C_2H_4 was adsorbed by the activated phase but that C_2H_6 was not adsorbed until phase transformation occurred.

value is the highest of all reported C_2H_6-selective porous materials, calculated as $\Delta Q = Q_{C2H6} - Q_{C2H4}$.

***In Situ* PXRD Experiments and Simulations.** To gain more insight into these gas-induced structural transformations, we collected *in situ* variable-pressure PXRD data for **X-dia-1-Ni** during C_2H_6 adsorption and desorption at 263 K (Figure 4A). Figure 4B shows no significant changes at the adsorption onset, consistent with the NP phase at low pressure. As the pressure was increased, characteristic NP diffraction peaks at 2θ = 5.76, 10.31, 17.34, and 18.65° gradually disappeared, whereas a diffraction peak at 7.27° characteristic of the LP phase appeared. During the desorption process, the PXRD pattern reverted to that of the NP phase, suggesting a reversible transformation between the NP and LP phases. *In situ* variable-pressure PXRD patterns were also recorded for C_2H_4 at 263 K to evaluate the host–guest interaction between C_2H_4 and the flexible MOF, as illustrated in Figure 4D. The corresponding C_2H_4 adsorption–desorption curves are shown in Figure 4C. The PXRD patterns remained unchanged during the C_2H_4 adsorption–desorption process, consistent with retention of the NP phase. During the initial stages of adsorption, the PXRD patterns of **X-dia-1-Ni** do not precisely match the calculated PXRD pattern of the NP phase. This discrepancy may arise from a transient phase that originated from the NP phase.[44] Details of the *in situ* variable-pressure PXRD experiments are provided in Figures S26–S29. Additionally, the structural models during *in situ* C_2H_6 variable-pressure PXRD (Figure 4B) were successfully refined by the Rietveld method using Expo2014 (Figures S30 and S31).[51] The calculated C_2H_6 adsorption binding sites for **X-dia-1-Ni** are shown in Figures S32 and S33. The results indicate that **X-dia-1-Ni** remains in the LP phase during C_2H_6 adsorption–desorption at approximately 100 kPa. The study's results demonstrate that ethane can induce the transition of **X-dia-1-Ni** from the NP phase to the LP phase. In addition, the phase transformation of **X-dia-1-Ni$_{0.89}$Co$_{0.11}$** was also studied by *in situ* variable-pressure PXRD, as shown in Figures S34 and S35. During the process of ethane adsorption, **X-dia-1-Ni$_{0.89}$Co$_{0.11}$** transitions from the NP phase to the LP phase. Conversely, during the ethane desorption process, **X-dia-1-Ni$_{0.89}$Co$_{0.11}$** reverts from the LP phase to the NP phase. Throughout the adsorption and desorption cycles of C_2H_4, **X-dia-1-Ni$_{0.89}$Co$_{0.11}$** consistently remains in the NP phase. This phenomenon is consistent with its adsorption isotherms for both C_2H_6 and C_2H_4.

Periodic density functional theory (DFT) calculations and Monte Carlo (MC) simulations were conducted to provide insight into the experimentally observed adsorption behavior and gating mechanism (Figure 5). The NP (**X-dia-1-Ni-NP**) and as-synthesized (**X-dia-1-Ni-LP**) crystal structures were used for the calculations. Higher energy was calculated for the binding of C_2H_4, relative to that of C_2H_6, with the NP phase (Table S3). Figure 5A,B shows stacked Pre-Opt and Post-Opt graphs that exhibit ring rotations of the ligand, indicating strong interactions between gas molecules and the framework. It appears that only one molecule of each adsorbate can occupy the space provided by the NP phase. The D_2h symmetry of C_2H_4 allows for a better fit compared to that of the bulkier C_2H_6 (Figure 5C,D). This could explain why C_2H_4 uptake was higher than that of C_2H_6 at pressures lower than 20 kPa, meaning that the NP phase is selective for C_2H_4 over C_2H_6 at low pressures. However, the better shape-fitting for C_2H_6 would be expected to drive conformational shifting, thus explaining the abrupt increase in the level of uptake (i.e., gate-

https://doi.org/10.1021/jacs.3c13117
J. Am. Chem. Soc. 2024, 146, 4153–4161

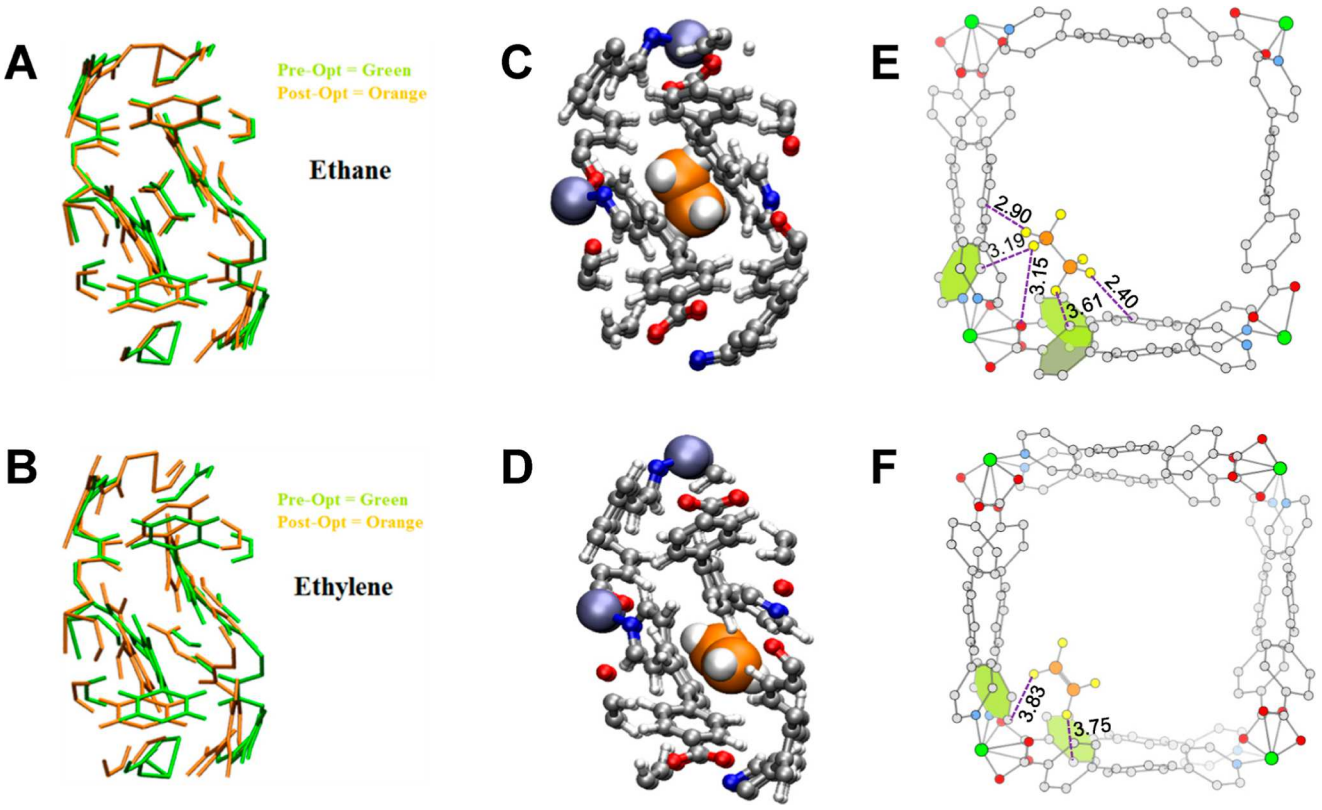

Figure 5. Stacked Pre-Opt and Post-Opt graphs exhibit ring rotations of the ligand, indicating strong interactions between (A) C_2H_6 and (B) C_2H_4 and the framework. Orthographic *c*-axis view of the optimized unit cell of **X-dia-1-Ni-NP** with (C) C_2H_6 and (D) C_2H_4 localized in the material, as obtained by using CP2K. Atom colors: C(MOF) = gray, C(C_2H_4/C_2H_6) = orange, H = white, N = blue, O = red, and Ni = lavender. (E) C_2H_6 and (F) C_2H_4 binding sites in **X-dia-1-Ni-LP**, as determined from molecular simulations. The C_2H_6/C_2H_4 molecules and **X-dia-1-Ni** are shown as ball-and-stick models (color codes: N, blue; Ni, green; O, red; H, yellow; and C, gray). The unit of distance in the figure is Å.

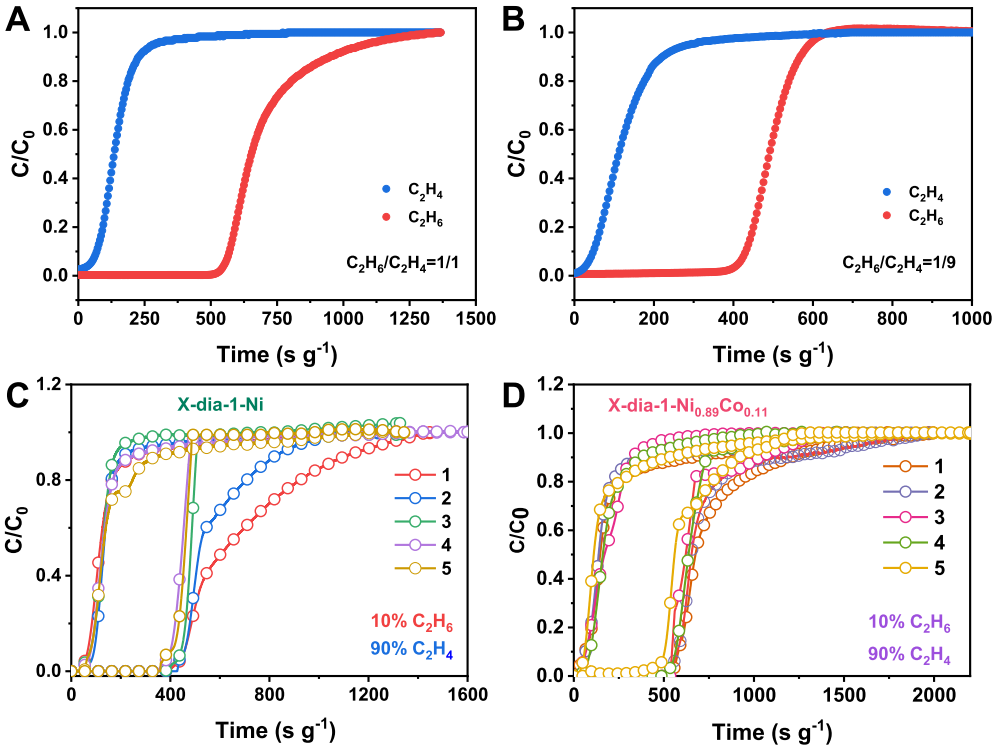

Figure 6. (A,B) Breakthrough curves for C_2H_4/C_2H_6 binary mixtures (1/1 and 1/9) measured at 263 K and 100 kPa. (C) Cyclic breakthrough separation experiments for C_2H_4/C_2H_6 (1/9) mixtures conducted with **X-dia-1-Ni** at 100 and 263 K. (D) Cyclic breakthrough separation experiments for C_2H_4/C_2H_6 (1/9) mixtures performed with **X-dia-1-Ni$_{0.89}$Co$_{0.11}$** at 100 kPa and 263 K.

https://doi.org/10.1021/jacs.3c13117
J. Am. Chem. Soc. 2024, 146, 4153−4161

opening) that was observed experimentally. The LP phase exhibits more favorable interactions and a higher binding energy for C_2H_6 than for C_2H_4. The energies for binding C_2H_6 and C_2H_4 with the LP phase were calculated to be −23.4 and −20.5 kJ mol^{-1}, respectively. The modeled structures at C_2H_6 and C_2H_4 saturation in the LP and NP phases are shown in Figures S36 and S37, respectively. Full optimizations of a single C_2H_6 or C_2H_4 molecule performed in a single unit cell of the NP phase for pre-optimizations and post-optimizations are shown in Figures S38 and S39. Grand canonical Monte Carlo (GCMC) simulations were also conducted to determine the binding sites for the gas molecules. The configuration calculated for the binding of C_2H_6 to **X-dia-1-Ni-LP** involved multiple C−H···O bonding distances of 2.40 and 3.61 Å (Figure 5E). On the other hand, C_2H_4 formed two C−H···O-bonds with distances of 3.75 and 3.83 Å (Figure 5F), longer than those of C_2H_6. Overall, the results of theoretical calculations provide mechanistic insight into the experimental results.

Dynamic Separations of C_2H_6/C_2H_4 Mixtures. To evaluate gas-mixture separation, breakthrough experiments were conducted at ambient pressure for binary gas mixtures of ethylene and ethane (1/1 or 1/9, v/v). In a typical experiment, a desolvated sample was activated at 313 K under a dynamic vacuum and then packed into a column. In the breakthrough curves, C_2H_4 first eluted as pure C_2H_4, while C_2H_6 eluted later (Figure 6A,B). To test the recyclability of **X-dia-1-Ni**, five cycles of breakthrough experiments were conducted with a two-component gas mixture (Figure 6C). **X-dia-1-Ni** maintained its C_2H_6/C_2H_4 separation performance through five cycling breakthrough experiments. In addition, we carried out similar experiments to assess the stability of **X-dia-1-$Ni_{0.89}Co_{0.11}$** over multiple breakthrough cycles (Figure 6D).

CONCLUSIONS

In summary, two flexible coordination networks, **X-dia-1-Ni** and **X-dia-1-$Ni_{0.89}Co_{0.11}$**, can exhibit benchmark performance for the separation of C_2H_6 from C_2H_4 through tuning the gate-opening pressure by temperature. This approach minimizes the coadsorption of ethylene while retaining high C_2H_6 uptake, leading to reverse C_2H_6/C_2H_4 separation. The gate-opening mechanism of **X-dia-1-Ni** and **X-dia-1-$Ni_{0.89}Co_{0.11}$** for the recognition of C_2H_6 was studied through *in situ* variable-pressure XRD studies and theoretical calculations. Importantly, the C_2H_6 uptake capacity for the LP phase of **X-dia-1-$Ni_{0.89}Co_{0.11}$** (273 K and 100 kPa) was determined to be 9.1 times higher than that for C_2H_4, far outperforming previously reported sorbents. High-purity C_2H_4 (≥99.9% pure) from C_2H_6/C_2H_4 mixtures was produced with a low-energy footprint. The present approach employs flexible MOFs that switch from an NP to an LP phase, and their metal contents can be adjusted to improve the separation efficiency for a specific gas mixture. Overall, this study indicates that flexible MOFs can be highly effective for the purification of C_2H_4.

ASSOCIATED CONTENT

Supporting Information

The Supporting Information is available free of charge at https://pubs.acs.org/doi/10.1021/jacs.3c13117.

Additional experimental details, materials, and methods, including sample synthesis, gas adsorption details, in situ PXRD method, modeling studies and theoretical calculation, FT-IR spectra, TGA curves, gas isotherms, *in situ* PXRD patterns, modeled structures, and a comparison of adsorbent performances (PDF)

AUTHOR INFORMATION

Corresponding Authors

Qing-Yuan Yang − *School of Chemical Engineering and Technology, Xi'an Jiaotong University, Xi'an 710049, China;* orcid.org/0000-0002-1742-2088; Email: qingyuan.yang@xjtu.edu.cn

Qingqing Guan − *Key Laboratory of Oil and Gas Fine Chemicals of Ministry of Education, College of Chemical Engineering, Xinjiang University, Urumqi 830017, China;* orcid.org/0000-0001-7574-191X; Email: 15545488@qq.com

Michael J. Zaworotko − *Department of Chemical Sciences, Bernal Institute, University of Limerick, Limerick V94 T9PX, Republic of Ireland;* orcid.org/0000-0002-1360-540X; Email: xtal@ul.ie

Authors

Shao-Min Wang − *School of Chemical Engineering and Technology, Xi'an Jiaotong University, Xi'an 710049, China*

Mohana Shivanna − *Department of Chemical Sciences, Bernal Institute, University of Limerick, Limerick V94 T9PX, Republic of Ireland*

Su-Tao Zheng − *School of Chemical Engineering and Technology, Xi'an Jiaotong University, Xi'an 710049, China*

Tony Pham − *Department of Chemistry, University of South Florida, Tampa, Florida 33620, United States;* orcid.org/0000-0001-5654-163X

Katherine A. Forrest − *Department of Chemistry, University of South Florida, Tampa, Florida 33620, United States;* Present Address: Department of Chemistry, North Carolina State University, 2700 Stinson Drive, Cox Hall 506, Raleigh, North Carolina 27607, United States

Brian Space − *Department of Chemistry, University of South Florida, Tampa, Florida 33620, United States;* Present Address: Department of Chemistry, North Carolina State University, 2700 Stinson Drive, Cox Hall 506, Raleigh, North Carolina 27607, United States

Susumu Kitagawa − *Institute for Integrated Cell-Material Sciences, Kyoto University Institute for Advanced Study, Kyoto University, Sakyo-ku, Kyoto 606-8501, Japan*

Complete contact information is available at: https://pubs.acs.org/10.1021/jacs.3c13117

Notes

The authors declare no competing financial interest.

ACKNOWLEDGMENTS

This work was financially supported by the China National Key R&D Program (2022YFB4003701) and the National Natural Science Foundation of China (no. 22371221). T.P., K.A.F., and B.S. acknowledge the National Science Foundation (Award no. 2154882). Computational resources were made available by an ACCESS Grant (no. CHE230105), Research Computing at the University of South Florida, and High-Performance Computing at North Carolina State University. Qingqing Guan acknowledges the Xinjiang Science Fund for Distinguished Young Scholars (2022D01E40). We thank Chang Huang at the Instrument Analysis Center of Xi'an

Jiaotong University for their assistance with single-crystal X-ray diffraction analyses.

REFERENCES

(1) Kitagawa, S.; Kondo, M. Functional micropore chemistry of crystalline metal complex-assembled compounds. *Bull. Chem. Soc. Jpn.* **1998**, *71*, 1739−1753.

(2) Horike, S.; Shimomura, S.; Kitagawa, S. Soft porous crystals. *Nat. Chem.* **2009**, *1*, 695−704.

(3) Schneemann, A.; Bon, V.; Schwedler, I.; Senkovska, I.; Kaskel, S.; Fischer, R. A. Flexible metal-organic frameworks. *Chem. Soc. Rev.* **2014**, *43*, 6062−6096.

(4) Behera, N.; Duan, J.; Jin, W.; Kitagawa, S. The chemistry and applications of flexible porous coordination polymers. *EnergyChem* **2021**, *3*, 100067.

(5) Mason, J. A.; Oktawiec, J.; Taylor, M. K.; Hudson, M. R.; Rodriguez, J.; Bachman, J. E.; Gonzalez, M. I.; Cervellino, A.; Guagliardi, A.; Brown, C. M.; et al. Methane storage in flexible metal-organic frameworks with intrinsic thermal management. *Nature* **2015**, *527*, 357−361.

(6) He, Y.; Zhou, W.; Qian, G.; Chen, B. Methane storage in metal-organic frameworks. *Chem. Soc. Rev.* **2014**, *43*, 5657−5678.

(7) Yuan, S.; Zou, L.; Li, H.; Chen, Y. P.; Qin, J.; Zhang, Q.; Lu, W.; Hall, M. B.; Zhou, H. C. Flexible zirconium metal-organic frameworks as bioinspired switchable catalysts. *Angew. Chem., Int. Ed.* **2016**, *55*, 10776.

(8) Pang, J.; Yuan, S.; Du, D.; Lollar, C.; Zhang, L.; Wu, M.; Yuan, D.; Zhou, H. C.; Hong, M. Flexible zirconium MOFs as bromine-nanocontainers for bromination reactions under ambient conditions. *Angew. Chem., Int. Ed.* **2017**, *56*, 14622.

(9) Taylor, M. K.; Runčevski, T.; Oktawiec, J.; Gonzalez, M. I.; Siegelman, R. L.; Mason, J. A.; Ye, J.; Brown, C. M.; Long, J. R. Tuning the adsorption-induced phase change in the flexible metal-organic framework Co(bdp). *J. Am. Chem. Soc.* **2016**, *138*, 15019−15026.

(10) Yu, M.-H.; Space, B.; Franz, D.; Zhou, W.; He, C.; Li, L.; Krishna, R.; Chang, Z.; Li, W.; Hu, T.-L.; et al. Enhanced gas uptake in a microporous metal-organic framework via a sorbate induced-fit mechanism. *J. Am. Chem. Soc.* **2019**, *141*, 17703−17712.

(11) Wang, H.; Warren, M.; Jagiello, J.; Jensen, S.; Ghose, S. K.; Tan, K.; Yu, L.; Emge, T. J.; Thonhauser, T.; Li, J. Crystallizing atomic xenon in a flexible MOF to probe and understand its temperature-dependent breathing behavior and unusual gas adsorption phenomenon. *J. Am. Chem. Soc.* **2020**, *142*, 20088−20097.

(12) Takashima, Y.; Martínez, V. M.; Furukawa, S.; Kondo, M.; Shimomura, S.; Uehara, H.; Nakahama, M.; Sugimoto, K.; Kitagawa, S. Molecular decoding using luminescence from an entangled porous framework. *Nat. Commun.* **2011**, *2*, 168.

(13) Yanai, N.; Kitayama, K.; Hijikata, Y.; Sato, H.; Matsuda, R.; Kubota, Y.; Takata, M.; Mizuno, M.; Uemura, T.; Kitagawa, S. Gas detection by structural variations of fluorescent guest molecules in a flexible porous coordination polymer. *Nat. Mater.* **2011**, *10*, 787−793.

(14) McKinlay, A.; Eubank, J.; Wuttke, S.; Xiao, B.; Wheatley, P.; Bazin, P.; Lavalley, J.-C.; Daturi, M.; Vimont, A.; De Weireld, G.; et al. Nitric oxide adsorption and delivery in flexible MIL-88 (Fe) metal-organic frameworks. *Chem. Mater.* **2013**, *25*, 1592−1599.

(15) Yang, F.; Xu, G.; Dou, Y.; Wang, B.; Zhang, H.; Wu, H.; Zhou, W.; Li, J.-R.; Chen, B. A flexible metal-organic framework with a high density of sulfonic acid sites for proton conduction. *Nat. Energy* **2017**, *2*, 877−883.

(16) Chang, Z.; Yang, D. H.; Xu, J.; Hu, T. L.; Bu, X. H. Flexible metal-organic frameworks: recent advances and potential applications. *Adv. Mater.* **2015**, *27*, 5432−5441.

(17) Yang, Q. Y.; Lama, P.; Sen, S.; Lusi, M.; Chen, K. J.; Gao, W. Y.; Shivanna, M.; Pham, T.; Hosono, N.; Kusaka, S.; et al. Reversible switching between highly porous and nonporous phases of an interpenetrated diamondoid coordination network that exhibits gate-opening at methane storage pressures. *Angew. Chem., Int. Ed.* **2018**, *57*, 5786−5791.

(18) Zhou, D.-D.; Zhang, J.-P. On the role of flexibility for adsorptive separation. *Acc. Chem. Res.* **2022**, *55*, 2966−2977.

(19) Wang, Z.; Sikdar, N.; Wang, S.-Q.; Li, X.; Yu, M.; Bu, X.-H.; Chang, Z.; Zou, X.; Chen, Y.; Cheng, P.; et al. Soft porous crystal based upon organic cages that exhibit guest-induced breathing and selective gas separation. *J. Am. Chem. Soc.* **2019**, *141*, 9408−9414.

(20) Zhang, X.-W.; Zhou, D.-D.; Zhang, J.-P. Tuning the gating energy barrier of metal-organic framework for molecular sieving. *Chem* **2021**, *7*, 1006−1019.

(21) Amghizar, I.; Vandewalle, L. A.; Van Geem, K. M.; Marin, G. B. New trends in olefin production. *Engineering* **2017**, *3*, 171−178.

(22) Sholl, D. S.; Lively, R. P. Seven chemical separations to change the world. *Nature* **2016**, *532*, 435−437.

(23) Ren, T.; Patel, M.; Blok, K. Olefins from conventional and heavy feedstocks: Energy use in steam cracking and alternative processes. *Energy* **2006**, *31*, 425−451.

(24) Li, J.-R.; Kuppler, R. J.; Zhou, H.-C. Selective gas adsorption and separation in metal-organic frameworks. *Chem. Soc. Rev.* **2009**, *38*, 1477−1504.

(25) Adil, K.; Belmabkhout, Y.; Pillai, R. S.; Cadiau, A.; Bhatt, P. M.; Assen, A. H.; Maurin, G.; Eddaoudi, M. Gas/vapour separation using ultra-microporous metal-organic frameworks: insights into the structure/separation relationship. *Chem. Soc. Rev.* **2017**, *46*, 3402−3430.

(26) Choi, B.-U.; Choi, D.-K.; Lee, Y.-W.; Lee, B.-K.; Kim, S.-H. Adsorption equilibria of methane, ethane, ethylene, nitrogen, and hydrogen onto activated carbon. *J. Chem. Eng. Data* **2003**, *48*, 603−607.

(27) Kim, J.; Lin, L.-C.; Martin, R. L.; Swisher, J. A.; Haranczyk, M.; Smit, B. Large-scale computational screening of zeolites for ethane/ethene separation. *Langmuir* **2012**, *28*, 11914−11919.

(28) Moulton, B.; Zaworotko, M. J. From molecules to crystal engineering: supramolecular isomerism and polymorphism in network solids. *Chem. Rev.* **2001**, *101*, 1629−1658.

(29) Eddaoudi, M.; Kim, J.; Rosi, N.; Vodak, D.; Wachter, J.; O'Keeffe, M.; Yaghi, O. M. Systematic design of pore size and functionality in isoreticular MOFs and their application in methane storage. *Science* **2002**, *295*, 469−472.

(30) Song, C.; Zheng, F.; Liu, Y.; Yang, Q.; Zhang, Z.; Ren, Q.; Bao, Z. Spatial distribution of nitrogen binding sites in metal-organic frameworks for selective ethane adsorption and one-step ethylene purification. *Angew. Chem., Int. Ed.* **2023**, *62*, No. e202313855.

(31) Pang, J.-J.; Ma, Z.-H.; Yang, Q.-Q.; Zhang, K.; Lian, X.; Huang, H.; Yao, Z.-Q.; Li, B.; Xu, J.; Bu, X.-H. A highly connected metal-organic framework with a specific nonpolar nanotrap for inverse ethane/ethylene separation. *Inorg. Chem. Front.* **2023**, *10*, 6407−6413.

(32) Zhao, S.; Yao, J.; Fan, Q.; Yuan, Y.; Tu, S.; Wu, Y.; Xia, Q. A highly stable yttrium-based metal-organic framework with two-fold interpenetrated and cage-like pore structure for one-step purification of ethylene from ethylene/ethane mixture. *Sep. Purif. Technol.* **2024**, *330*, 125256.

(33) Nie, H.-X.; Yu, M.-H.; Gao, Q.; Krishna, R.; Chang, Z. Customized pore fluorination in a microporous metal-organic framework for efficient ethane/ethylene separation. *Sep. Purif. Technol.* **2023**, *327*, 124967.

(34) Mersmann, A.; Fill, B.; Hartmann, R.; Maurer, S. The potential of energy saving by gas-phase adsorption processes. *Chem. Eng. Technol.* **2000**, *23*, 937−944.

(35) Ye, Y.; Xie, Y.; Shi, Y.; Gong, L.; Phipps, J.; Al-Enizi, A. M.; Nafady, A.; Chen, B.; Ma, S. A microporous metal-organic framework with unique aromatic pore surfaces for high performance C_2H_6/C_2H_4 separation. *Angew. Chem., Int. Ed.* **2023**, *62*, No. e202302564.

(36) Wu, X.-Q.; Zhang, P.-D.; Zhang, X.; Liu, J.-H.; He, T.; Yu, J.; Li, J.-R. Ethylene purification in a metal-organic framework over a wide temperature range via pore confinement. *Green Energy Environ.* **2023**, *8*, 1703−1710.

(37) Mukherjee, S.; Sensharma, D.; Chen, K.-J.; Zaworotko, M. J. Crystal engineering of porous coordination networks to enable

https://doi.org/10.1021/jacs.3c13117
J. Am. Chem. Soc. 2024, 146, 4153−4161

separation of C2 hydrocarbons. *Chem. Commun.* **2020**, *56*, 10419−10441.
(38) Liu, W.; Geng, S.; Li, N.; Wang, S.; Jia, S.; Jin, F.; Wang, T.; Forrest, K. A.; Pham, T.; Cheng, P.; et al. Highly robust microporous metal-organic frameworks for efficient ethylene purification under dry and humid conditions. *Angew. Chem., Int. Ed.* **2023**, *62*, No. e202217662.
(39) Jiang, S.; Li, J.; Feng, M.; Chen, R.; Guo, L.; Xu, Q.; Chen, L.; Shen, F.; Zhang, Z.; Yang, Y.; et al. Hydrophobic paraffin-selective pillared-layer MOFs for olefin purification. *J. Mater. Chem. A* **2022**, *10*, 24127−24136.
(40) Li, L.; Lin, R.-B.; Krishna, R.; Li, H.; Xiang, S.; Wu, H.; Li, J.; Zhou, W.; Chen, B. Ethane/ethylene separation in a metal-organic framework with iron-peroxo sites. *Science* **2018**, *362*, 443−446.
(41) Yang, H.; Wang, Y.; Krishna, R.; Jia, X.; Wang, Y.; Hong, A. N.; Dang, C.; Castillo, H. E.; Bu, X.; Feng, P. Pore-space-partition-enabled exceptional ethane uptake and ethane-selective ethane-ethylene separation. *J. Am. Chem. Soc.* **2020**, *142*, 2222−2227.
(42) Yang, Y.; Li, L.; Lin, R.-B.; Ye, Y.; Yao, Z.; Yang, L.; Xiang, F.; Chen, S.; Zhang, Z.; Xiang, S.; et al. Ethylene/ethane separation in a stable hydrogen-bonded organic framework through a gating mechanism. *Nat. Chem.* **2021**, *13*, 933−939.
(43) Gucuyener, C.; van den Bergh, J.; Gascon, J.; Kapteijn, F. Ethane/ethene separation turned on its head: selective ethane adsorption on the metal-organic framework ZIF-7 through a gate-opening mechanism. *J. Am. Chem. Soc.* **2010**, *132*, 17704−17706.
(44) Nikolayenko, V. I.; Castell, D. C.; Sensharma, D.; Shivanna, M.; Loots, L.; Forrest, K. A.; Solanilla-Salinas, C. J.; Otake, K. ichi; Kitagawa, S.; Barbour, L. J.; et al. Reversible transformations between the non-porous phases of a flexible coordination network enabled by transient porosity. *Nat. Chem.* **2023**, *15*, 542−549.
(45) Lin, R.-B.; Wu, H.; Li, L.; Tang, X.-L.; Li, Z.; Gao, J.; Cui, H.; Zhou, W.; Chen, B. Boosting ethane/ethylene separation within isoreticular ultramicroporous metal-organic frameworks. *J. Am. Chem. Soc.* **2018**, *140*, 12940−12946.
(46) Ehrling, S.; Mendt, M.; Senkovska, I.; Evans, J. D.; Bon, V.; Petkov, P.; Ehrling, C.; Walenszus, F.; Pöppl, A.; Kaskel, S. Tailoring the adsorption-induced flexibility of a pillared layer metal-organic framework DUT-8 (Ni) by cobalt substitution. *Chem. Mater.* **2020**, *32*, 5670−5681.
(47) Ehrling, S.; Senkovska, I.; Bon, V.; Evans, J. D.; Petkov, P.; Krupskaya, Y.; Kataev, V.; Wulf, T.; Krylov, A.; Vtyurin, A.; et al. Crystal size versus paddle wheel deformability: selective gated adsorption transitions of the switchable metal-organic frameworks DUT-8 (Co) and DUT-8 (Ni). *J. Mater. Chem. A* **2019**, *7*, 21459−21475.
(48) Miura, H.; Bon, V.; Senkovska, I.; Ehrling, S.; Bönisch, N.; Mäder, G.; Grünzner, S.; Khadiev, A.; Novikov, D.; Maity, K.; et al. Spatiotemporal design of the metal-organic framework DUT-8 (M). *Adv. Mater.* **2023**, *35*, 2207741.
(49) Wang, S.-M.; Shivanna, M.; Lama, P.; Yang, Q.-Y.; Barbour, L. J.; Zaworotko, M. J. Metal doping to control gate opening and increase methane working capacity in isostructural flexible diamondoid networks. *ChemSusChem* **2023**, *16*, No. e202300069.
(50) Sacconi, L. The influence of geometry and donor-atom set on the spin state of five-coordinate cobalt (II) and nickel (II) complexes. *Coord. Chem. Rev.* **1972**, *8*, 351−367.
(51) Altomare, A.; Cuocci, C.; Giacovazzo, C.; Moliterni, A.; Rizzi, R.; Corriero, N.; Falcicchio, A. EXPO2013: a kit of tools for phasing crystal structures from powder data. *J. Appl. Crystallogr.* **2013**, *46*, 1231−1235.

https://doi.org/10.1021/jacs.3c13117
J. Am. Chem. Soc. 2024, 146, 4153−4161